Device

Article

Self-aligning EPM connector: A versatile solution for adaptive and multi-modal interfaces

Graphical abstract

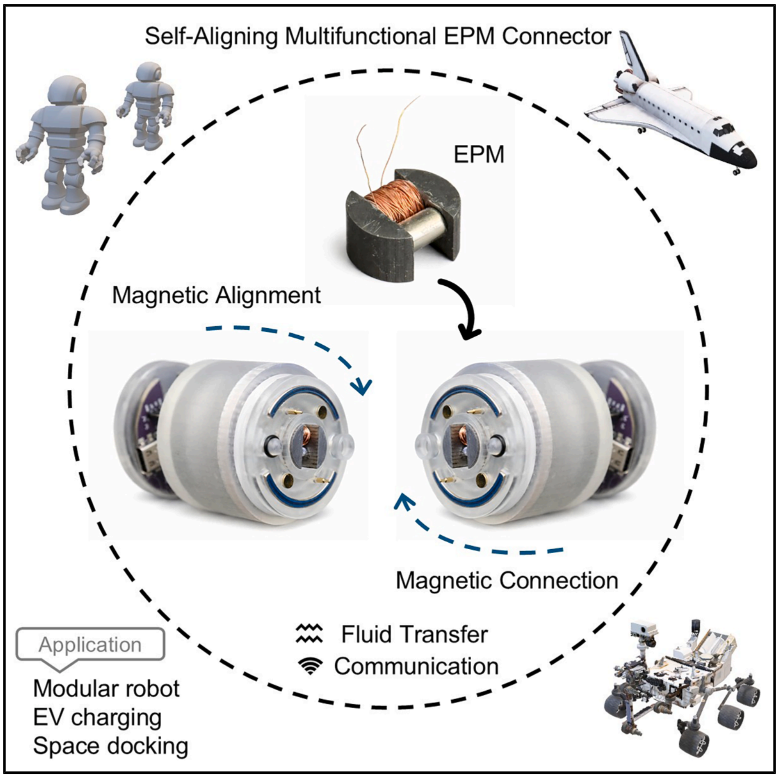

Highlights

- Self-aligning EPM connector enables reversible, power-free mechanical coupling
- Integrated interface supports fluid transfer and digital communication
- Flexible architecture tolerates misalignment, rotation, and dynamic motion
- Demonstrated reliable docking and transfer on mobile robotic platforms

Authors

Bingchao Wang, Adam A. Stokes

Correspondence

b.wang-57@sms.ed.ac.uk (B.W.),
adam.stokes@ed.ac.uk (A.A.S.)

In brief

A self-aligning electropermanent magnet connector enables reversible docking with mechanical coupling, fluid transfer, and digital communication in a single interface. The connector operates without continuous power, tolerates misalignment and motion, and supports reliable system-level integration, offering a versatile solution for modular robotics, automated docking, and resource-transfer applications.

3 **Develop**
Prototype with demonstrated applications
in relevant environment

Wang & Stokes, 2026, Device *4*, 101068
April 17, 2026
https://doi.org/10.1016/j.device.2026.101068

CellPress

Please cite this article in press as: Wang and Stokes, Self-aligning EPM connector: A versatile solution for adaptive and multi-modal interfaces, Device (2026), https://doi.org/10.1016/j.device.2026.101068

Device

CellPress
OPEN ACCESS

Article

Self-aligning EPM connector: A versatile solution for adaptive and multi-modal interfaces

Bingchao Wang[1,*] and Adam A. Stokes[1,2,3,*]
[1]Soft Systems Group, The School of Engineering, the University of Edinburgh, EH9 3FF Edinburgh, UK
[2]Senior author
[3]Lead contact
*Correspondence: b.wang-57@sms.ed.ac.uk (B.W.), adam.stokes@ed.ac.uk (A.A.S.)
https://doi.org/10.1016/j.device.2026.101068

THE BIGGER PICTURE Modern robotic and automated systems increasingly rely on connectors that can reliably transfer multiple resources—such as mechanical load, fluids, power, and data—while operating under misalignment, motion, and limited energy budgets. Conventional connectors often require precise positioning, continuous power, or complex mechanical latching, which limits their robustness and scalability in dynamic or unstructured environments.

This work presents a self-aligning electropermanent magnet (EPM) connector that addresses these challenges through a compact, energy-efficient, and multifunctional design. By combining magnetic self-alignment, reversible mechanical coupling, sealed fluid transfer, and digital communication within a single interface, the connector enables reliable docking without continuous power consumption. The use of EPMs allows strong attachment when needed while maintaining a passive, power-free holding state during operation. Integrated mechanical compliance further allows the connector to tolerate angular, lateral, and axial misalignments, as well as relative rotation after docking. Beyond demonstrating individual functions, this study shows how a single connector architecture can support coordinated mechanical, fluidic, and electronic interactions under both static and mobile conditions. The system-level demonstration highlights the relevance of this approach for real-world scenarios such as modular robotics, autonomous docking, electric-vehicle charging interfaces, and future space or off-world resource transfer systems.

SUMMARY

This paper presents a multifunctional connector based on electropermanent magnet (EPM) technology that addresses key limitations of existing mechanical, magnetic, and hybrid interfaces. The connector unifies self-alignment, mechanical coupling, fluid transfer, and digital communication within a compact stereolithography (SLA)-printed structure. Experimental evaluation confirms reliable magnetic alignment, consistent fluid-transfer performance across different operating modes, and stable data exchange through an integrated electronic interface. The mechanical architecture provides substantial flexibility, allowing the connector to accommodate axial, angular, and lateral misalignments while maintaining secure engagement and synchronized motion after docking. An optimized EPM design, in which the coil is wound exclusively around the AlNiCo element, improves magnetic efficiency and reduces energy requirements during switching. Collectively, these capabilities establish the connector as a robust and versatile solution for modular robotic platforms, automated docking systems, electric-vehicle charging interfaces, and space-relevant applications requiring precise, adaptive, and low-power interconnections.

INTRODUCTION

In modular robotics and numerous everyday systems, performance effectiveness increasingly relies on innovative connector technologies. Connectors designed for self-alignment facilitate rapid reconfiguration, robust integration, and adaptability, enabling systems to swiftly respond to dynamic or unstructured environments. Modular robots particularly benefit from these connectors, as they allow flexible assembly, simplified maintenance, and reliable module integration, essential for adapting to complex tasks and uncertain conditions.[1–4] Beyond robotics, versatile self-aligning connectors play critical roles in everyday applications, including electric vehicle (EV) charging interfaces, automated vacuum docking stations, and integrated smart

Please cite this article in press as: Wang and Stokes, Self-aligning EPM connector: A versatile solution for adaptive and multi-modal interfaces, Device (2026), https://doi.org/10.1016/j.device.2026.101068

home systems. Such connectors significantly enhance docking efficiency, minimize manual intervention, and improve reliability during daily operations.[5] Moreover, in challenging environments such as space exploration, reliable self-aligning connectors facilitate spacecraft docking, satellite servicing, and the modular assembly of space stations, demanding precise autonomous operations under constrained and unpredictable conditions.[6,7] As systems become more interconnected and multifunctional, connectors capable of supporting simultaneous electrical, data, and fluidic transfers are increasingly essential.[8]

Controllable connection mechanisms are typically categorized as mechanical, magnetomechanical, or electromagnetic.[9] Traditional module interconnections generally utilize mechanical latching mechanisms due to their reliability in ensuring secure coupling. Representative examples include the HiGen connector, which features four radial hooks that rotate and mechanically interlock with complementary hooks, achieving strong and repeatable connections.[10] Additionally, the SINGO connector employs an actively driven spiral gear mechanism, providing substantial alignment tolerance and error correction capabilities.[11] The X-Claw connector, another notable mechanical design, uses an active gripping mechanism combined with self-alignment features, enabling high acceptance angles and multiple attachment orientations between modules.[12] Despite their reliability and stability, mechanical connectors' dependence on motors and active components introduces spatial constraints, limiting their applicability in compact or resource-constrained environments.

To address some of these limitations, many connector designs incorporate permanent magnets for effective alignment and coupling.[13,14] For instance, the EMERGE modular robot integrates magnetic connectors directly into module mating surfaces, enabling efficient alignment and secure attachment.[15] Similarly, robotic units equipped with ring-shaped permanent magnets facilitate precise self-alignment during connection.[16] Although effective for alignment, these permanent magnet-based connectors inherently lack active self-detachment capabilities, restricting their versatility in dynamic and reconfigurable scenarios.

Electropermanent magnets (EPMs) have increasingly become the connector of choice due to their rapid switching capability, energy efficiency, and ability to maintain strong connections without continuous power consumption.[17,18] Prominent examples include the EP-Face connector, which employs a planar array of EPMs for rapid switching and robust holding strength, significantly enhancing module connectivity performance.[19] Similarly, the SMORES-EP system uses EPM-based connectors on multiple faces, facilitating versatile and reliable robotic reconfigurations and highlighting advantages in modular flexibility and scalability.[20] Another notable approach is the M-Blocks robotic modules, which leverage EPMs to enable self-assembly and autonomous mobility by dynamically adjusting magnetic polarity for controlled attachment and detachment.[21,22] Despite these advancements, current EPM-based connectors still exhibit limitations, such as reduced performance under shear and torsional loads,[19] and insufficient multifunctionality—particularly regarding fluidic or hybrid connections.[20] Consequently, significant potential exists for developing enhanced EPM connectors that combine multifunctional coupling and mechanical robustness. Recent advances in modular robotic connectors emphasize integrating fluidic, electrical, and communication functionalities within a unified interface.[23] Several standardized interfaces incorporating fluid or air transfer have emerged to enable these functionalities effectively. The PAC (power, air, communication) connector facilitates seamless resource sharing by combining pneumatic transfer capabilities with robust mechanical and magnetic locking mechanisms for secure and reversible module connections.[24] Another innovation is the standard interface for robotic manipulation (SIROM), developed by SENER Aeroespacial, which integrates mechanical coupling, electrical interfaces, refueling, thermal transfer, and data communication into a compact, unified solution.[25–27] Similarly, GMV's ASSIST system employs a dedicated berthing fixture with integrated fluid connectors, facilitating zero-force docking and secure fluid transfer between spacecraft.[27,28] However, these connector designs generally lack intrinsic self-alignment capabilities, relying instead on external systems or precise manual alignment, significantly limiting their effectiveness in dynamic or autonomous scenarios, where rapid and accurate self-alignment is crucial.[9] Orbit Fab's rapidly attachable fluid transfer interface (RAFTI) employs alignment markers known as fiducials to facilitate docking by providing visual cues during proximity operations, thus reducing docking complexity.[29] Despite improving docking precision, visual-based alignment systems such as RAFTI's fiducials possess inherent limitations, particularly in low-visibility conditions such as poor lighting or obstructed views, potentially hindering accurate visual detection and alignment.[30,31]

To address these limitations, we introduce a novel self-aligning connector incorporating an EPM system (Figure 1A) to achieve multifunctionality in mechanical connection, fluid transfer, and data communication. Our proposed connector architecture is designed specifically to overcome existing limitations, targeting modular soft robotic systems and extending to broader commercial applications, including EV charging ports and domestic robotic systems such as household mopping robots. Key features of our design include (1) a compact and integrated mechanical structure fabricated via stereolithography (SLA)-based 3D printing technology, equipped with EPMs, bearings, springs, and other components for robust and reliable mechanical connections; (2) embedded electronic control provided by a custom-designed printed circuit board (PCB) with an integrated STM32 microcontroller, facilitating the feasibility of digital communication via universal asynchronous receiver-transmitter (UART); (3) an internal isolation design that ensures complete sealing of internal mechanical and electronic components from transported fluids; (4) mechanical decoupling capability that enables relative rotation, precise self-alignment, and accommodation of minor positional misalignments between connected modules; (5) low-energy EPM activation requiring only 0.3 J per switching event—achieved via a 30-V, 10-A pulse lasting 1 ms (Figures S2 and S3)—supporting energy-efficient operation; and (6) versatile fluid transfer functionality capable of both unidirectional and bidirectional fluid exchange, applicable to modular robotics, EV charging systems, household robotics, and space applications requiring reliable fluid management and robust mechanical interconnections.

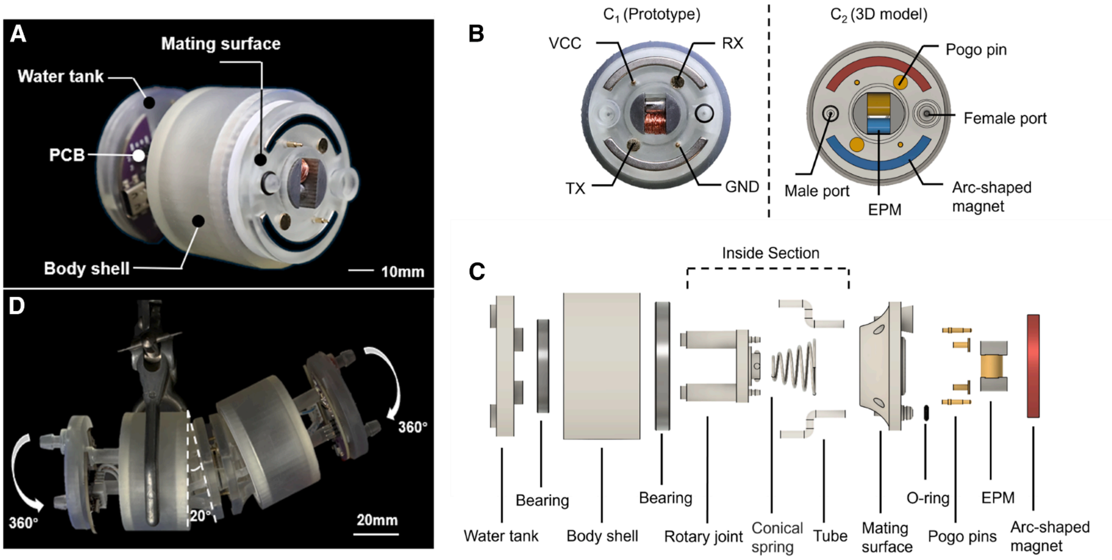

Figure 1. Integrated structure and mechanical flexibility of the self-aligning fluidic EPM connector

(A) Overall structure of the fluidic EPM connector. Scale bar, 10 mm.

(B) Magnetic and fluidic interface layout.

(C) Exploded view of the connector architecture.

(D) Mechanical flexibility of the connector during rotation and bending. Scale bar, 20 mm.

RESULTS

EPM connector design

The conception of the proposed EPM connector involves integrating two different pole arc-shaped permanent magnets and one EPM embedded within the mating surface (Figure 1B). As the two mating surfaces approach, the connector autonomously aligns through rotational movements enabled by integrated bearings, driven by the combined effects of magnetic attraction and repulsion, thus achieving precise self-alignment (Figure S4; Video S1). Within a certain proximity, the EPMs attract each other to firmly secure the mating surfaces. Consequently, the male port on the C_1 interface aligns and connects with the corresponding female port on the C_2 interface, and similarly, the male port on the C_2 interface connects to the female port on the C_1 interface, successfully establishing a reliable fluidic channel upon connector engagement. Simultaneously, the pogo pins on the mating surfaces establish one-to-one connections. Demagnetizing the EPMs results in the disconnection of the mating surfaces, separating the fluid channels and pogo-pin connections (Figure S3).

The EPM connector consists of four primary parts: (1) an EPM, (2) a conical spring (Metrol, UK), (3) two bearings (Simply Bearings, UK), and (4) a fluid channel system. The fluid is delivered from the water tank through a rotary joint, guided by a silicone tube into the connector's internal channel (Figure 1C), and finally exits through the mating surface, thereby completing the fluid pathway within the connector. This constitutes the complete fluid channel system within the connector. The integration of the conical spring and bearings allows flexible coupling, accommodating angular misalignments up to 20° (Figure 1D). Furthermore, the internal structure of the connector permits 360° rotation relative to the body shell, enabling synchronized rotation of both connectors upon engagement, significantly enhancing adaptability and robustness in dynamic operational environments.

The water tank of each EPM connector includes two independent fluid inlets, internally forming isolated fluid transmission paths that allow for the simultaneous transfer of two different fluids without cross-contamination. When two EPM connectors are coupled, the system supports three distinct modes of fluid transfer (Figure 2A): (1) parallel unidirectional dual-channel fluidic transfer, where fluid flows simultaneously through two separate parallel channels from one connector into the other (Video S4); (2) dual-channel fluidic transfer, where fluids flow simultaneously in opposite directions through two separate and isolated channels between connectors (Video S5); and (3) single-loop fluidic transfer, in which fluid enters through one connector, passes into and through the other connector, and returns via a separate pathway, creating a closed-loop circuit (Video S6). Throughout all modes, the fluid pathways remain fully isolated to ensure fluid purity and prevent contamination from internal components. In the inside section, a conical spring connects the mating surface to the rotary joint, while bearings are positioned at both ends of the body shell—one mounted around the rotary joint and the other forming a line contact with the mating surface (Figure S7). The combined action of the conical spring and the bearings enables synchronized rotational motion among the mating surface, the rotary joint, and the water tank while also allowing a degree of relative flexibility between the connected units (Video S2). The fabrication of the water tank, body shell, rotary joint, and mating surface in the EPM connector is carried out using SLA 3D printing technology.

Please cite this article in press as: Wang and Stokes, Self-aligning EPM connector: A versatile solution for adaptive and multi-modal interfaces, Device (2026), https://doi.org/10.1016/j.device.2026.101068

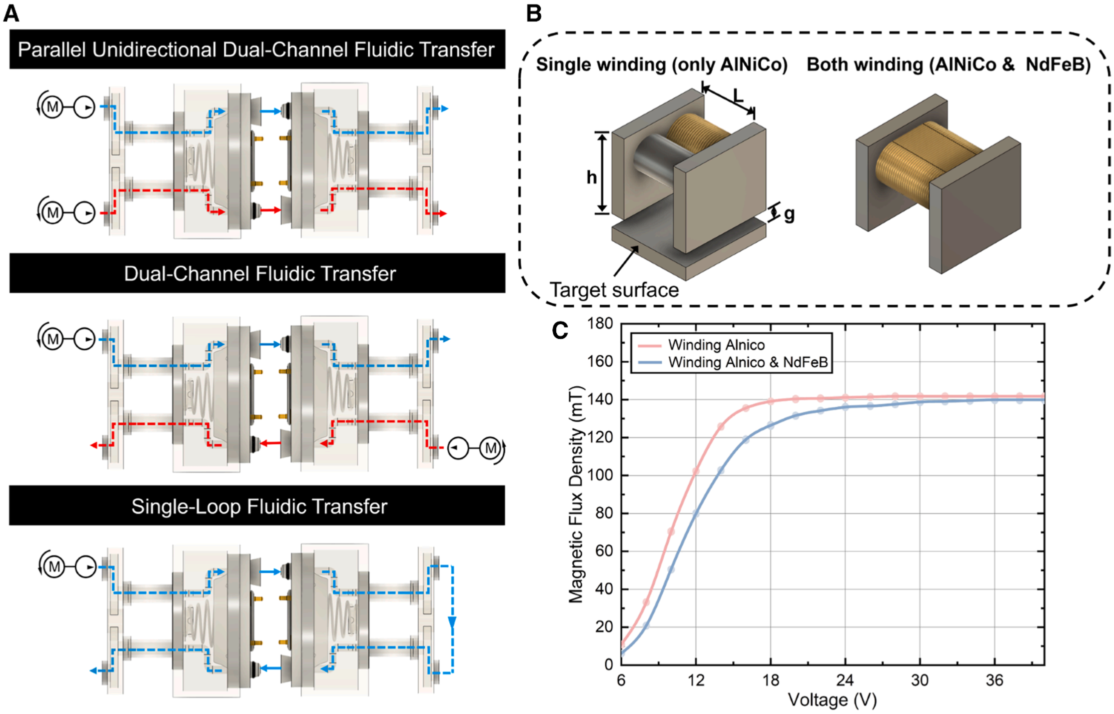

Figure 2. Fluidic transfer modes and EPM coil-winding configurations with magnetic performance comparison

(A) Three operational fluidic transfer modes of the connector: parallel unidirectional dual-channel transfer, bidirectional dual-channel transfer, and single-loop circulation.

(B) Schematic illustration of the two EPM coil-winding strategies: single winding (AlNiCo only) and both winding (AlNiCo and NdFeB).

(C) Comparison of magnetic flux density for different coil-winding configurations. Each data point represents the mean magnetic flux density obtained from five repeated measurements at the same voltage ($n = 5$). The variance across repeated trials was small, resulting in overlapping points that appear as a single marker. Solid lines represent the mean trend for each winding configuration.

The connectors employ pogo pins to deliver both electrical power and UART-based data exchange under the control of onboard STM32 microcontrollers. Their symmetrical arrangement allows flexible multi-orientation connectivity, improving adaptability during assembly. The mating surfaces include supply voltage (VCC), ground (GND), transmit (TX), and receive (RX) pins, which automatically establish the corresponding electrical links upon engagement. The spring-loaded structure ensures reliable contact, thereby supporting stable operation and consistent signal transmission. To confirm the feasibility of digital communication across the connector, two identical STM32 boards were interconnected through the pogo-pin interface to establish a bidirectional UART link (115,200 bps, 8-N-1). The master board periodically transmitted “PING” messages, and the slave board successfully replied with “ACK” signals, verifying end-to-end data transfer under dynamic conditions (Video S10; Figures S10 and S11). Onboard light-emitting diodes (LEDs), controlled by the STM32 microcontrollers and mounted on the rotating PCB located above the water tank, provide intuitive visual feedback regarding connection and communication status. A red LED briefly illuminates during data transmission between connectors, while a green LED remains continuously on once a mechanical and electrical connection is established, together providing clear visual confirmation of communication activity and stable connectivity. The PCB, along with the integrated STM32 controllers and LEDs, rotates synchronously with the water tank and pogo-pin connector assembly, ensuring stable operation throughout dynamic operation (Figure S8; Video S3). The EPM was actuated by a 30-V external direct current (DC) power supply through an H-bridge driver, with polarity switching controlled by an Arduino. This configuration enabled the required high-current pulse (30 V, 10 A, 1 ms) without exceeding the limits of the control board (Figure S9). Because the pulse is very short in duration, it does not impose noticeable thermal or electrical disturbance on the onboard electronics. In future integrated systems, the EPM can be actuated directly from an onboard battery through the H-bridge driver. Because the required activation is a short, 1-ms pulse, a small local energy-storage capacitor is sufficient to supply the transient peak current without loading the battery or disturbing the control electronics. This approach keeps the system compact while ensuring reliable EPM switching in practical deployments.

EPM design and optimization

An EPM consists of two rod magnets with different coercivities: a hard magnet made of NdFeB and a soft magnet made of AlNiCo, along with end caps. A coil is positioned to generate a magnetic field that selectively changes the polarization of the soft magnet when pulsed with current. The magnetic force at the end caps is enabled when both magnets are polarized in the same direction and disabled when their polarizations oppose each other.[32]

Please cite this article in press as: Wang and Stokes, Self-aligning EPM connector: A versatile solution for adaptive and multi-modal interfaces, Device (2026), https://doi.org/10.1016/j.device.2026.101068

EPMs have been extensively utilized across various fields, employing diverse fabrication methods. Generally, two common approaches exist for coil placement in EPM fabrication (Figure 2B). In the first method, the coil is wound around both the AlNiCo and NdFeB magnets.[33–35] In the second method, the coil is wound exclusively around the AlNiCo magnet.[36] In the EPM connector, the force generated by the EPM serves as the coupling force between connectors. To estimate this force, we adopt the magnetic circuit model proposed by Knaian,[32] making several modifications to suit our specific application.

The general expression for the magnetomotive force (MMF) balance in the EPM magnetic circuit can be written as

$$NI = 2H_g g + \sum_i \sigma_i H_i L_i, \qquad \text{(Equation 1)}$$

where H_i and L_i are the magnetic field intensity and effective length of each segment, respectively, and $\sigma_i \in \{+1, -1\}$ is a sign factor that depends on the relative orientation of the magnetization of the segment with respect to the reference direction of the magnetic circuit. A segment with $\sigma_i = +1$ acts as an MMF-consuming element (demagnetizing), while a segment with $\sigma_i = -1$ acts as an MMF-contributing element (magnetizing). This formulation highlights that the role of each magnet in the circuit is not fixed but depends on its polarization state relative to the circuit.

For the purpose of analysis, we first consider a representative case in which both the AlNiCo and NdFeB magnets act as MMF-consuming elements, i.e., $\sigma_{Al} = \sigma_{Nd} = +1$. Under this assumption, the effective MMFs available at the air gaps become

$$\mathcal{F}_A = NI - H_{\mathrm{Al}} L_{\mathrm{Al}} \text{ and} \qquad \text{(Equation 2)}$$

$$\mathcal{F}_B = NI - H_{\mathrm{Al}} L_{\mathrm{Al}} - H_{\mathrm{Nd}} L_{\mathrm{Nd}}, \qquad \text{(Equation 3)}$$

where $\mathcal{F}_A$ corresponds to the effective MMF in the single-winding configuration (coil wound exclusively around the AlNiCo magnet) and $\mathcal{F}_B$ corresponds to the effective MMF in the both-winding configuration (coil wound around both the AlNiCo and NdFeB magnets).

While the total MMF (NI) generated by the coil remains constant in both scenarios, the efficiency with which it is utilized exhibits substantial variation. In configuration A, nearly all of the supplied MMF is directed toward the AlNiCo magnet, which has relatively low coercivity and can be effectively remagnetized. In configuration B, however, part of the MMF is consumed within the NdFeB segment. Due to its high coercivity, this MMF does not contribute to switching and is effectively wasted, thereby reducing the usable MMF for remagnetizing the AlNiCo magnet. This difference in MMF utilization underpins the superior efficiency of the single-winding strategy.

For convenience, the effective MMF delivered to the air gaps is denoted as $\mathcal{F}_{\mathrm{eff}}$, which takes the value of either $\mathcal{F}_A$ or $\mathcal{F}_B$ depending on the winding configuration. Once $\mathcal{F}_{\mathrm{eff}}$ is determined, the magnetic field intensity H_g and the magnetic flux density B_g in the air gaps can be calculated as

$$H_g = \frac{\mathcal{F}_{\mathrm{eff}}}{2g}, B_g = \mu_0 H_g, \qquad \text{(Equation 4)}$$

where H_g is the magnetic field intensity in the air gap (A/m), $\mathcal{F}_{\mathrm{eff}}$ is the effective MMF delivered to both air gaps (ampere-turns), g is the air-gap thickness (m), B_g is the resulting magnetic flux density (T), and μ_0 is the permeability of free space.

This relationship clearly indicates that the magnetic flux density in the air gap is directly proportional to the effective MMF provided by the coil and inversely proportional to the total air-gap length. Thus, the coil-winding configuration significantly influences the resultant flux density. Practically, increasing the coil turns while minimizing internal MMF losses within the magnet segments effectively enhances the magnetic field strength achievable in the air gap.

To validate the theoretical predictions regarding the influence of coil-winding strategies on magnetic flux density, systematic experiments were conducted using EPM prototypes. Each prototype consisted of an AlNiCo 5 rod magnet (7 mm in length and 5 mm in diameter), a Grade N40 NdFeB disk magnet of identical dimensions, and precision-machined Q235 steel end caps (13 × 11 × 3 mm). Two coil configurations were fabricated: configuration A, in which a coil of 130 turns of a 0.20-mm-diameter copper wire was wound exclusively around the AlNiCo magnet, and configuration B, in which a coil of 130 turns of a 0.22-mm-diameter copper wire encompassed both the AlNiCo and NdFeB magnets. The coil resistances were adjusted to approximately 2.0 Ω to ensure equivalent MMF (NI) under identical voltage conditions, thereby allowing direct and fair comparison between the two winding strategies.

The experimental results (Figure 2C) demonstrate that the single-winding configuration consistently achieved higher magnetic flux density and reached saturation more rapidly across all tested voltage levels. For each input voltage, the magnetic flux density was measured five times. The reported values correspond to the mean of these trials. By contrast, the both-winding configuration yielded lower flux density, as part of the coil MMF was expended across the NdFeB segment, whose high coercivity prevented effective remagnetization. These findings confirm the theoretical analysis: although the total MMF is identical in both cases, the single-winding design utilizes it more efficiently by directing nearly all of the MMF toward switching the AlNiCo magnet. Consequently, the single-winding strategy was selected in this project as the more energy-efficient coil design for prototype development and further validation.

Based on both analytical considerations and experimental validation, the EPM employed in the fluidic connector was constructed using an AlNiCo 5 rod magnet (7 × 5 mm, Guys Magnets, UK) paired with a Grade N35 NdFeB disk magnet (Radial Magnets, USA). A 120-turn excitation coil of 35-AWG enameled copper wire (0.15 mm diameter) was wound around the AlNiCo rod, resulting in a measured resistance of 3.0 Ω (Figure 3A). The end caps, fabricated from Q235 steel, were designed with a circular-segment contact face of approximately 48.9 mm^2. This geometry was selected following a comparative assessment against a rectangular end cap of similar size. While a larger nominal area could theoretically reduce the flux density ($B \approx \Phi/A$), experimental pull-off tests demonstrated that the circular-segment design achieves stronger and more robust

Please cite this article in press as: Wang and Stokes, Self-aligning EPM connector: A versatile solution for adaptive and multi-modal interfaces, Device (2026), https://doi.org/10.1016/j.device.2026.101068

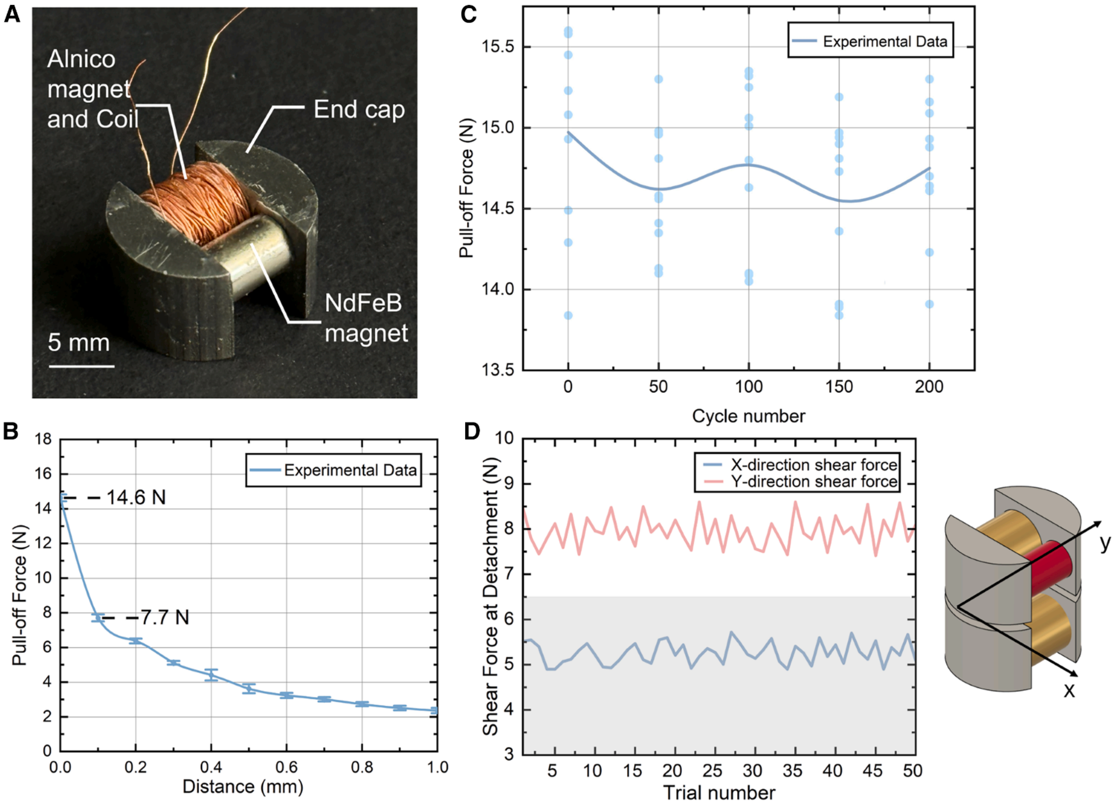

Figure 3. Magnetic performance, durability, and shear behavior of the electropermanent magnet

(A) Circular-segment-shaped end-cap electropermanent magnet (EPM). Scale bar, 5 mm.

(B) Pull-off force vs. air gap for the EPM. Each scatter point represents an individual measurement, and ten repeated trials were performed at each gap distance ($n = 10$). Error bars represent standard deviation. The solid curve represents the mean pull-off force across the ten measurements.

(C) Pull-off force stability over 200 activation cycles.

(D) Shear detachment forces in the x and y directions of the EPM end cap ($n = 50$ per direction).

magnetic coupling across practical micro-gaps due to reduced edge fringing and improved flux utilization. Detailed force-gap measurements and the full comparison procedure are provided in the supplemental information (Figure S12).

To evaluate the overall holding capability of the connector, we measured the dependence of the pull-off force on controlled micro-gaps using a tensile testing configuration (Figure 3B). Pull-off force measurements were repeated ten times at each air-gap distance. For each distance, the mean value was used to generate the plotted trend curve. Gap distances from 0 to 1 mm were introduced using stacked paper shims in increments of 0.1 mm, and the force required to separate two opposing EPMs was recorded. The holding force was found to decrease rapidly: the value at a 0.1-mm gap was already approximately half of the zero-gap force, and the force continued to decline until reaching about 2.3 N at a gap of 1 mm. These observations demonstrate the pronounced sensitivity of EPM holding force to small variations in gap size and support the use of a rounded end-cap geometry, which provides more stable performance under slight misalignments or surface irregularities. Additional fabrication and testing details are presented in the supplemental information (Figures S1, S5, and S6).

EPM magnetic performance and durability

To evaluate the long-term magnetic stability of the EPM, a 200-cycle durability test was conducted in which two opposing EPMs were repeatedly activated and separated. Each cycle consisted of a 30-V, 1-ms forward-current pulse, which magnetized the AlNiCo element and produced magnetic engagement, followed by a 30-V, 1-ms reverse-current pulse to demagnetize the AlNiCo and induce separation. This forward-reverse pulse pair constituted one complete activation cycle.

Pull-off force measurements were taken every 50 cycles (i.e., at cycle numbers 0, 50, 100, 150, and 200). At each checkpoint, ten independent pull-off trials were conducted under identical alignment and loading conditions to assess repeatability. In Figure 3C, each scatter point represents one of the ten repeated measurements at a given checkpoint, while the solid line connects the mean values to illustrate the overall trend of the holding force. The results show that the pull-off force remained stable across the 200-cycle test, staying within approximately 14–15.5 N with no observable downward trend. Because the connector's holding force is primarily generated by the magnetic attraction between the two EPMs, the measured EPM pull-off force directly reflects the effective connection strength between the connector halves.

Please cite this article in press as: Wang and Stokes, Self-aligning EPM connector: A versatile solution for adaptive and multi-modal interfaces, Device (2026), https://doi.org/10.1016/j.device.2026.101068

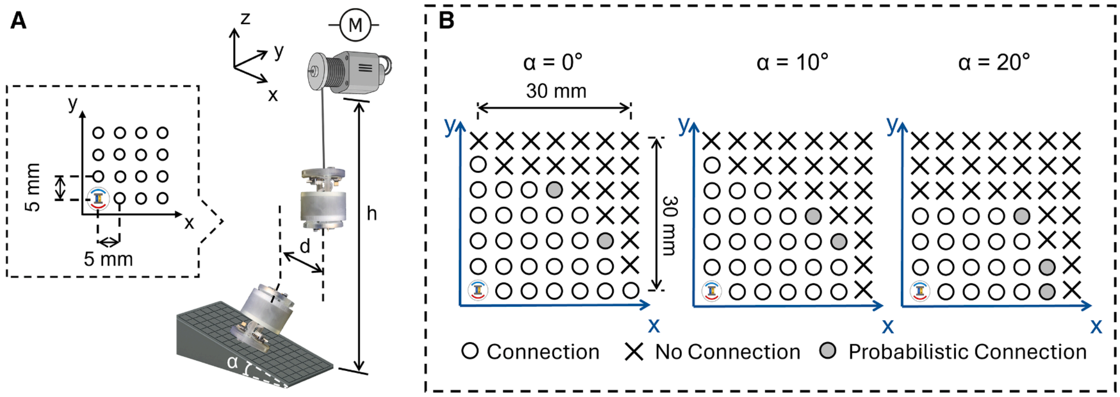

Figure 4. Experimental setup and alignment outcome maps for assessing the connector's self-alignment performance under varying tilt angles

(A) Experimental setup for evaluating magnetic self-alignment, including the 7 × 7 test grid, adjustable tilt angle α, and vertical approach trajectory.

(B) Self-alignment outcomes across the 7 × 7 grid for tilt angles of $\alpha = 0^\circ$, 10°, and 20°. Circles denote successful connections, crosses indicate failures, and gray circles represent probabilistic outcomes (1–2 successes out of 3 trials). Across three repeated sweeps, the spatial patterns remained consistent, with probabilistic points concentrated near the transition boundary between successful and failed alignment.

To further characterize the magnetic coupling behavior of the EPM interface, the lateral shear resistance between two opposing EPMs was evaluated along two orthogonal directions of the circular-segment end cap (Figure 3D). The magnets were placed in direct contact, and a horizontal force was applied until detachment. Across 50 trials per direction, the *x*-direction shear force remained around 5–5.6 N, whereas the *y*-direction shear force was consistently higher at 7.8–8.6 N. This directional difference reflects the geometry of the end caps and the asymmetric flux distribution of the arc-shaped permanent magnets. These shear measurements confirm that the EPM interface maintains reliable lateral stability and is capable of withstanding realistic off-axis perturbations during connection.

Self-alignment performance

The connector employs magnetic attraction-repulsion, assisted by bearings, to achieve self-alignment. Its performance was evaluated using an improved method based on Zoltan's approach.[37] One connector (C_1) was fixed on a platform with an adjustable tilt angle (α), while the other (C_2) was lowered vertically at 3 mm/s from a height of 30 mm (Figure 4A). The test space was defined as a 7 × 7 grid with 5-mm increments in both the *x* and *y* directions.

To assess repeatability, the complete 49-point grid experiment was independently repeated three times ($n = 3$ sweeps). Based on the aggregated outcomes, each grid point was classified into one of three categories: (1) connection, where all three trials resulted in successful attachment; (2) no connection, where all trials failed; and (3) probabilistic connection, where 1 or 2 out of 3 trials succeeded. The probabilistic category typically appeared near the boundary between successful and failed regions, highlighting the stochastic nature of marginal alignment conditions.

At $\alpha = 0^\circ$, the connector achieved reliable alignment within a 30 × 25-mm region (59.1% success rate). Increasing the tilt to $\alpha = 10^\circ$ reduced the fully successful region to approximately 25 × 25 mm, yielding a 55.1% overall success rate. At $\alpha = 20^\circ$, successful alignment was restricted to a narrower 25 × 15 mm region, with correspondingly more probabilistic points, reducing the success rate to 44.9% (Figure 4B).

These results indicate that although alignment performance decreases with increasing tilt angle, the connector consistently maintains robust self-alignment capability under moderate angular misalignment, with stochastic partial successes occurring only near the operational boundary.

Fluid transfer performance

When the connectors mate, the male fluidic ports align magnetically with the corresponding female ports, achieving precise engagement. Concurrently, an O-ring positioned on the male fluidic ports is compressed under the magnetic force generated by the EPM, effectively sealing the interface between the male and female ports. This tight sealing mechanism ensures reliable fluid transfer by preventing leakage during operation.

Fluid transmission efficiency was assessed by measuring the flow rates at both the inlet and outlet of the connector. The experimental setup incorporated two Sensirion SLF3S-4000B (Sensirion, Switzerland) flow sensors positioned at the inlet and outlet, respectively. Fluid delivered by a water pump passed through the inlet sensor, entered the connector's water tank, traveled through the internal channels, exited via the outlet sensor, and finally returned to the reservoir (Figure 5). Two fluid-transfer modes were examined: single-loop transfer and dual-channel transfer. Each mode was tested at three different inlet flow rates. Every experiment ran for 2 min, and a 30-s segment of steady-state data was sampled for analysis. Before each experiment, the fluid lines were drained to avoid residual effects and ensure consistent measurements.

The connector's fluid-transfer performance was quantified using the fluidic efficiency (η), defined as the ratio between the outlet and inlet volumetric flow rates:

$$\eta = \frac{Q_{\text{out}}}{Q_{\text{in}}} \times 100\%. \quad \text{(Equation 5)}$$

Please cite this article in press as: Wang and Stokes, Self-aligning EPM connector: A versatile solution for adaptive and multi-modal interfaces, Device (2026), https://doi.org/10.1016/j.device.2026.101068

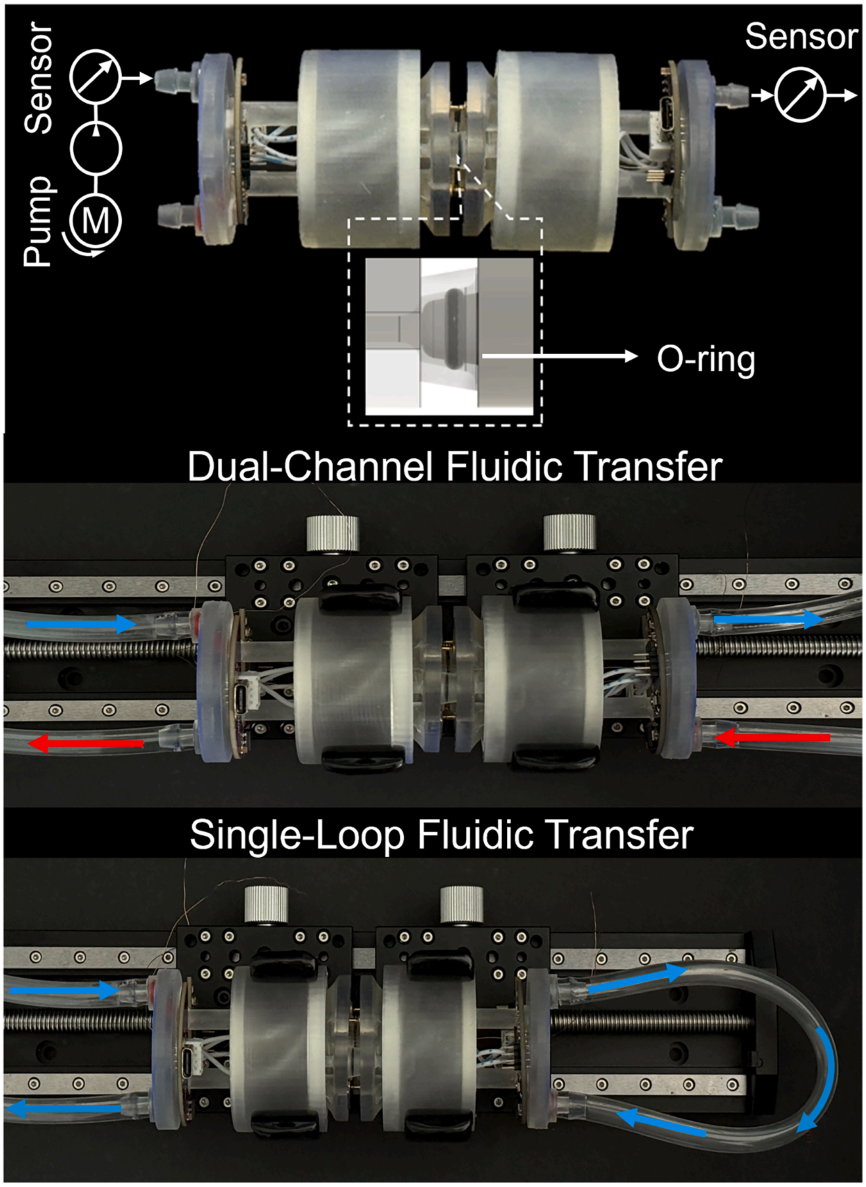

Figure 5. Diagram of EPM connector configuration and fluid transfer experiment

Here, Q_{in} and Q_{out} denote the measured inlet and outlet flow rates. This metric provides a clear and reproducible means of evaluating the connector's performance. In addition to sensor accuracy (±5% full scale for the SLF3S-4000B), minor measurement uncertainty may arise from short-term fluctuations in pump delivery and the occasional presence of micro-bubbles within the tubing. Such bubbles can transiently perturb the thermal mass-flow readings and cause small fluctuations in the measured values, typically on the order of ±2–3 mL/min for both the inlet and outlet measurements. Across all tests, these variations resulted in an estimated efficiency uncertainty on the order of ±1.5%–2%, which does not affect the overall performance trends reported in this study.

A representative data point illustrates the computation of efficiency. For an inlet flow rate of Q_{in} = 80 mL/min and a corresponding outlet flow rate of Q_{out} = 49 mL/min, substitution into Equation 5 gives

$$\eta = \frac{49}{80} \times 100\% = 61.25\%.$$

This example reflects the procedure used throughout the analysis.

Single-loop fluidic transfer exhibited consistent behavior across the tested inlet flow rates. At an inlet flow of 80 mL/min, the outlet flow stabilized at approximately 49 mL/min, producing an efficiency of around 61% (Figure 6A). Increasing the inlet flow to 90 mL/min elevated the outlet flow to roughly 56 mL/min, maintaining an efficiency of approximately 62% (Figure 6B). The highest inlet flow of 100 mL/min yielded an outlet flow of about 65 mL/min, corresponding to an efficiency of approximately 65% (Figure 6C). The modest variation in efficiency across all tests indicates stable connector performance. The reduced efficiency observed in the single-loop mode is explained by the fluid traversing the water tank and internal channels twice, which amplifies hydraulic losses and therefore lowers the overall efficiency.

The dual-channel fluidic transfer mode demonstrated significantly improved fluid transfer efficiency compared to the single-loop mode. At an inlet flow rate of 102 mL/min, the outlet flow rate was closely matched at about 98 mL/min, resulting in an efficiency of around 95% (Figure 6D). Increasing the input to 140 mL/min led to a proportional rise in the outlet flow rate to approximately 136 mL/min, maintaining efficiency at about 97% (Figure 6E). At the highest tested input of 175 mL/min, the outlet flow rate averaged approximately 170 mL/min, corresponding to an efficiency consistently around 98% (Figure 6F). These results indicate highly stable and efficient performance in the dual-channel fluidic transfer mode.

In summary, these experiments demonstrate that the dual-channel fluidic transfer mode significantly enhances fluid transfer efficiency compared to the single-loop mode. Both modes maintained stable performance across varying inlet flow rates, indicating the reliable functionality of the connector under different operational conditions. The connector's internal flow path consists of narrow channels and several geometric

Please cite this article in press as: Wang and Stokes, Self-aligning EPM connector: A versatile solution for adaptive and multi-modal interfaces, Device (2026), https://doi.org/10.1016/j.device.2026.101068

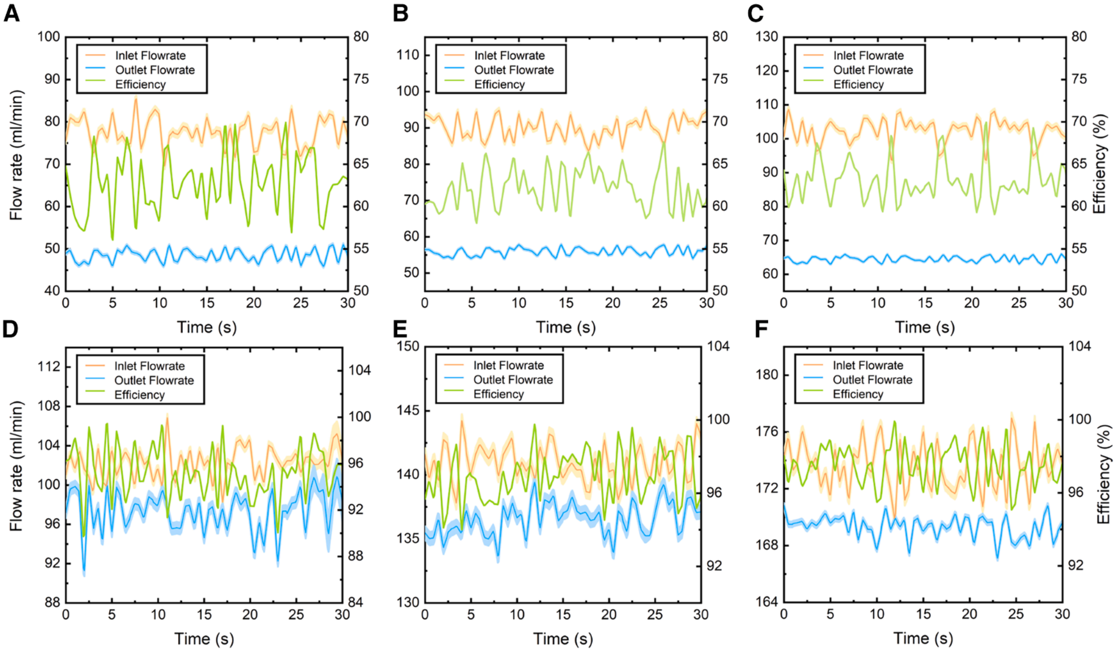

Figure 6. Flow rate and efficiency data in single-loop and dual-channel fluidic transfer modes

(A–C) Flow rate and efficiency in single-loop fluidic transfer mode at an inlet flow of (A) 80, (B) 90, and (C) 100 mL/min.

(D–F) Flow rate and efficiency in dual-channel fluidic transfer mode at an inlet flow of (D) 102, (E) 140, and (F) 175 mL/min.

transitions, including inlet narrowing, internal turns, and a recirculation region within the water tank. As the fluid travels through these features, it encounters substantial viscous resistance that slows down the flow, resulting in a measurable reduction in flow rate. This reduction reflects hydraulic drag within the device rather than leakage, and the connector consistently maintains stable and predictable performance across all tested conditions.

EPM connector for mechanical connection

For applications primarily focused on mechanical connections, the EPM connector provides an ideal solution by integrating flexible coupling, EPM technology, and magnetic self-alignment capabilities (Figure 7A). Structurally, the connector is divided into two primary sections—upper and lower—connected by a conventional compression spring.

The upper section consists of an upper housing, an internal rotor, an EPM, arc-shaped magnets, a bearing, an end cover, and embedded permanent magnets. A bearing facilitates the rotation of the internal rotor relative to the outer casing. The strategically positioned EPM and arc-shaped magnets within the internal rotor enable automatic magnetic alignment, significantly simplifying the coupling process. The lower section comprises a lower housing, a bottom rotor, another bearing, and additional embedded permanent magnets. These magnets interact with those embedded in the upper section, effectively connecting the upper and lower sections together and reinforcing secure alignment upon engagement. A conventional compression spring mechanically links the upper and lower sections. In contrast to the conical spring employed in fluidic connectors, this conventional spring provides a simpler and potentially more flexible mechanical response, accommodating a greater range of positional variations and misalignments.

When activated, the EPM generates a strong yet reversible magnetic force, enabling the spring to extend or retract smoothly in response to attraction or repulsion. Rapid demagnetization returns the connector promptly to its original state, guaranteeing consistent and reliable mechanical alignment. This design allows rapid connection and disconnection without continuous current, greatly reducing energy consumption. Additionally, the bearings support relative rotational movement, and the spring's compliance facilitates flexible alignment, making the connector particularly suitable for modular systems requiring adaptability and mechanical flexibility.

Characterization of the EPM connector's mechanical coupling capability

Mechanical connection flexibility

To comprehensively characterize the mechanical coupling performance and flexibility of the connector, several tests were conducted (Figure 7B; Video S7). The axial extension test demonstrated the connector's capacity for substantial axial deformation, achieving a maximum extension of 20 mm when subjected to a gradually increasing tensile force. In the angular flexibility test, the connector accommodated a significant angular misalignment, reaching a maximum bending angle of approximately 30° when a bending moment was applied. Additionally, the lateral offset test confirmed the connector's tolerance to horizontal displacement, successfully maintaining coupling at an offset of up to 6 mm. Lastly, the maximum connection distance test evaluated the robustness of the

Please cite this article in press as: Wang and Stokes, Self-aligning EPM connector: A versatile solution for adaptive and multi-modal interfaces, Device (2026), https://doi.org/10.1016/j.device.2026.101068

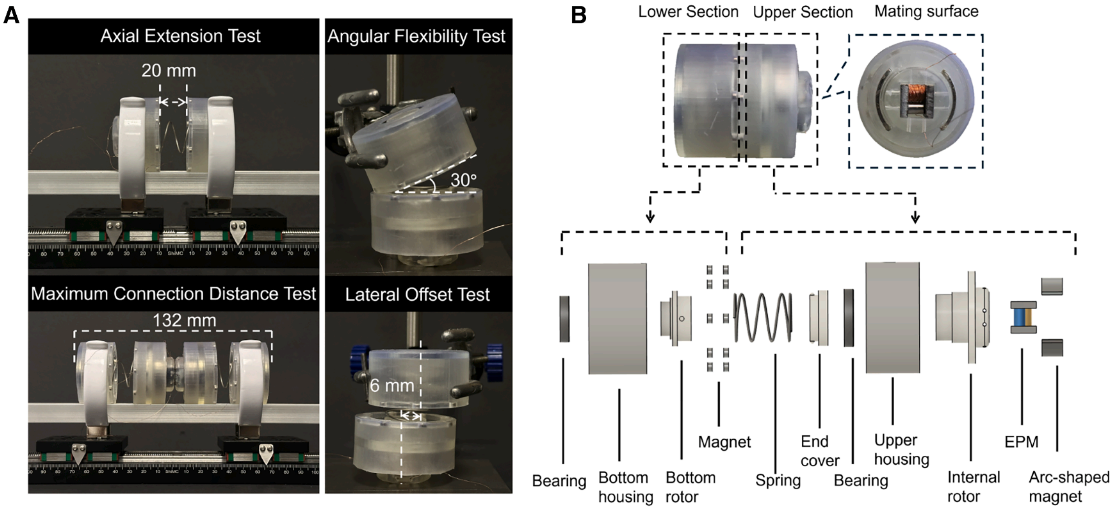

Figure 7. Mechanical flexibility characterization and structural architecture of the EPM mechanical connector

(A) Mechanical flexibility tests of the connector, including axial extension, angular flexibility, maximum connection distance, and lateral offset.

(B) Structural architecture of the EPM mechanical connector, showing the lower and upper sections, mating surface, and detailed exploded view of internal components.

connector under extended conditions, showing that connectors could remain securely coupled over distances of up to 132 mm. These results collectively highlight the connector's substantial mechanical adaptability and robust coupling capability across various alignment scenarios. Repeated trials exhibited minimal variation (<5%), indicating robust mechanical repeatability.

System-level demonstration on mobile platforms

To explore how the proposed connector could operate in mobility-driven scenarios such as those encountered in planetary surface missions, a system-level demonstration was carried out using two custom wheeled platforms (Figures S13 and S14). One platform was actively driven using a handheld controller to emulate a mobile robotic unit, whereas the other platform remained stationary and unpowered, serving as a passive service node. Each platform carried an EPM connector and an independent fluid tank.

During operation, the driven platform approached the passive platform with natural lateral and angular offsets induced by movement. As the connectors entered proximity, magnetic interactions initiated the self-alignment process, allowing the mating surfaces to rotate and converge until a stable docking configuration was achieved. Once the connectors were engaged, the dual-channel fluid pathway enabled liquid transfer between the two platforms. Importantly, the connection remained sealed and functional even while the platforms were in motion, demonstrating that the connector maintains mechanical coupling, magnetic stability, and fluidic integrity under dynamic conditions.

A sequence illustrating this process, including the approach, self-alignment, docking, synchronized motion after attachment, and subsequent fluid transfer, is shown in Figure 8, and the full demonstration is provided in Video S9. This experiment highlights the connector's capability to support autonomous docking and resource exchange in mobile and unstructured environments, reinforcing its potential for applications such as extraterrestrial resource handling, modular robotic servicing, and distributed surface infrastructure.

DISCUSSION

The multifunctional EPM connector advances existing connector technologies by integrating magnetic self-alignment, mechanical coupling, fluid transfer, and digital communication in a compact form. EPM activation enables reversible attachment without continuous power, and the optimized coil configuration enhances magnetic efficiency and switching reliability. The connector also shows strong mechanical adaptability, accommodating positional variations while maintaining stable engagement. Its structure supports synchronized rotation after docking, and SLA-based fabrication enables low-cost and scalable production. Fluid-transfer tests confirmed reliable sealing and stable operation under both static and dynamic conditions. Digital communication across the pogo-pin interface was also validated. In addition, durability tests demonstrated consistent magnetic performance under repeated activation, indicating long-term reliability.

Overall, the connector provides a versatile and robust interface suitable for modular robotics and autonomous docking scenarios where misalignment, motion, and low-power requirements are critical considerations (Videos S8 and S9).

Limitations and future work

Although the connector demonstrates notable performance improvements, several limitations remain to be addressed. Firstly, while fluid transfer performance is efficient for typical fluids such as water, challenges arise when handling high-density or particulate-containing fluids, potentially causing internal channel blockages and significantly reducing transfer efficiency.

Please cite this article in press as: Wang and Stokes, Self-aligning EPM connector: A versatile solution for adaptive and multi-modal interfaces, Device (2026), https://doi.org/10.1016/j.device.2026.101068

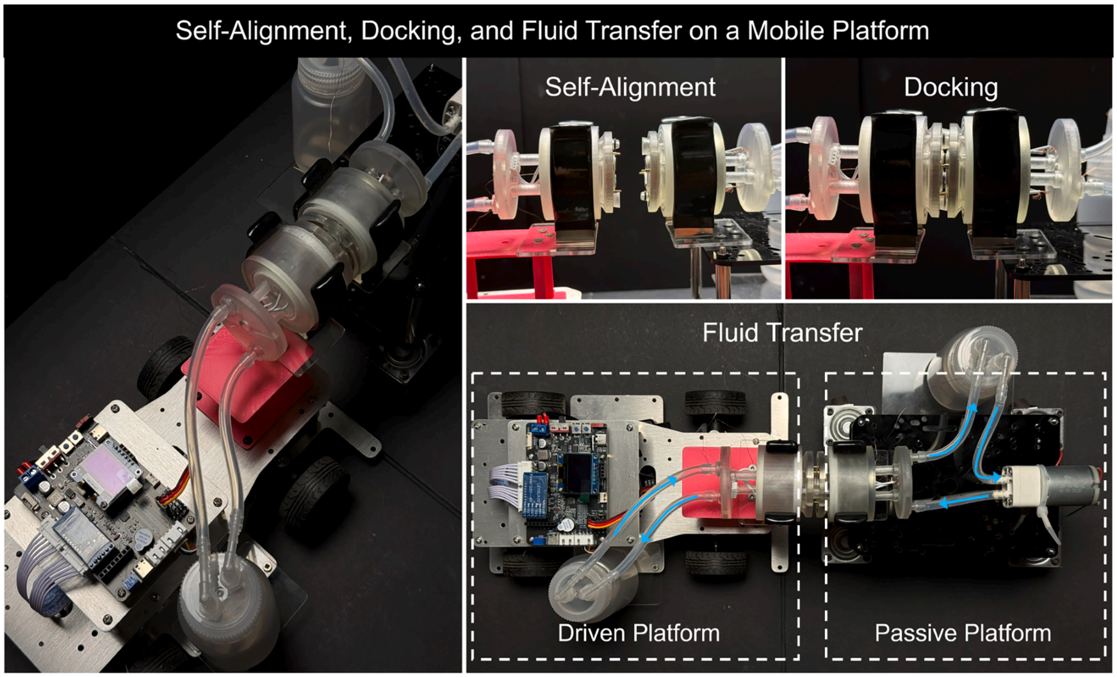

Figure 8. System-level demonstration of autonomous docking and fluid transfer using the EPM connector

Secondly, the EPM activation relies on short, high-current pulses, necessitating robust external circuitry capable of delivering instantaneous high-energy demands.

Secondly, while the EPM provides a strong normal holding force, its shear resistance is comparatively lower, making the connection more susceptible to lateral disturbances that may induce premature detachment. This limitation stems from the fact that the magnetic flux is optimized for normal attraction rather than transverse stability. Future improvements could focus on enhancing shear robustness through modest geometric refinements to the end caps or by integrating lightweight passive features such as shallow alignment guides or friction-enhancing surface textures, which can provide additional lateral support without compromising the reversible nature of the EPM connection.

METHODS

EPM connector design and fabrication

The EPM connector was designed in Autodesk Fusion and 3D printed on an SLA 3D printer (Formlabs Form 3) using Clear Resin v.4 material. Printed parts include the water tank, body shell, rotary joint, and mating surface (STL files of the components are available and described in more detail in the text and supplemental information).

The tube inside the EPM connector is a silicone tube with a 3 mm outer diameter and a 2 mm inner diameter. The dimensions of the two bearings are 35 × 44 × 5 and 25 × 32 × 4 mm, respectively.

EPM design and fabrication

The EPM fabrication details are in the supplemental information.

RESOURCE AVAILABILITY

Lead contact

Requests for further information and resources should be directed to and will be fulfilled by the lead contact, Adam A. Stokes (adam.stokes@ed.ac.uk).

Materials availability

This study did not generate new unique reagents.

Data and code availability

All data and source code underlying this study are available from the corresponding author upon reasonable request.

ACKNOWLEDGMENTS

This research received no specific grant from any funding agency in the public, commercial, or not-for-profit sector. The authors are grateful to the members of the lab for their constructive feedback and assistance throughout the study.

AUTHOR CONTRIBUTIONS

Conceptualization, B.W.; methodology, B.W.; writing – original draft, B.W. and A.A.S.; writing – review & editing, A.A.S.; supervision, A.A.S.

DECLARATION OF INTERESTS

The authors declare no competing interests.

DECLARATION OF GENERATIVE AI AND AI-ASSISTED TECHNOLOGIES IN THE WRITING PROCESS

During the preparation of this work, the authors used ChatGPT-4o (OpenAI) to enhance the clarity and language quality of the manuscript. The tool was also used to assist in drafting the initial description of the experimental objective associated with Figure 4A. All AI-assisted content was carefully reviewed, revised, and validated by the authors, who take full responsibility for the integrity and accuracy of the final publication.

SUPPLEMENTAL INFORMATION

Supplemental information can be found online at https://doi.org/10.1016/j.device.2026.101068.

Received: October 30, 2025
Revised: January 20, 2026
Accepted: January 22, 2026

REFERENCES

1. Yim, M., Shen, W.M., Salemi, B., Rus, D., Moll, M., Lipson, H., Klavins, E., and Chirikjian, G.S. (2007). Modular self-reconfigurable robot systems [grand challenges of robotics]. IEEE Robot. Autom. Mag. *14*, 43–52. https://doi.org/10.1109/MRA.2007.339623.
2. Zhang, C., Zhu, P., Lin, Y., Jiao, Z., and Zou, J. (2020). Modular soft robotics: Modular units connection mechanisms and applications. Adv. Intell. Syst. *2*, 1900166. https://doi.org/10.1002/aisy.202000032.
3. Saab, W., Racioppo, P., and Ben-Tzvi, P. (2019). A review of coupling mechanism designs for modular reconfigurable robots. Robotica *37*, 378–403. https://doi.org/10.1017/S0263574718001066.
4. Seo, J., Paik, J., and Yim, M. (2019). Modular reconfigurable robotics. Annu. Rev. Control Robot. Auton. Syst. 2, 63–88.
5. Song, G., Wang, H., Zhang, J., and Meng, T. (2011). Automatic docking system for recharging home surveillance robots. IEEE Trans. Consum. Electron. *57*, 428–435. https://doi.org/10.1109/TCE.2011.5955176.
6. Flores-Abad, A., Ma, O., Pham, K., and Ulrich, S. (2014). A review of space robotics technologies for on-orbit servicing. Prog. Aero. Sci. *68*, 1–26. https://doi.org/10.1016/j.paerosci.2014.03.002.
7. Papadopoulos, E., Aghili, F., Ma, O., and Lampariello, R. (2021). Robotic manipulation and capture in space: A survey. Front. Robot. AI *8*, 686723. https://doi.org/10.3389/frobt.2021.686723. https://www.frontiersin.org/journals/robotics-and-ai/articles/10.3389/frobt.2021.686723.
8. Arif, S.M., Lie, T.T., Seet, B.C., Ayyadi, S., and Jensen, K. (2021). Review of electric vehicle technologies, charging methods, standards and optimization techniques. Electronics *10*, 1910. https://doi.org/10.3390/electronics10161910. https://www.mdpi.com/2079-9292/10/16/1910.
9. Eckenstein, N., and Yim, M. (2014). Area of acceptance for 3d self-aligning robotic connectors: Concepts, metrics, and designs. In 2014 IEEE International Conference on Robotics and Automation (ICRA), pp. 1227–1233. https://doi.org/10.1109/ICRA.2014.6907010.
10. Parrott, C., Dodd, T.J., and Groß, R. (2014). Higen: A high-speed self-reconfigurable modular robot connector. In 2014 IEEE/RSJ International Conference on Intelligent Robots and Systems (IROS), pp. 3926–3932. https://doi.org/10.1109/IROS.2014.6943114.
11. Shen, W.M., Kovac, R., and Rubenstein, M. (2009). Singo: A single-end-operative and genderless connector for self-reconfiguration, self-assembly and self-healing. In 2009 IEEE International Conference on Robotics and Automation, pp. 4253–4258. https://doi.org/10.1109/ROBOT.2009.5152408.
12. Cong, J., and Fitch, R.C. (2011). The x-claw self-aligning connector for self-reconfiguring modular robots. URL: https://api.semanticscholar.org/CorpusID:6691184.
13. Zhao, L., Wu, Y., Blanchet, J., Perroni-Scharf, M., Huang, X., Booth, J., Kramer-Bottiglio, R., and Balkcom, D. (2022). Soft lattice modules that behave independently and collectively. IEEE Robot. Autom. Lett. *7*, 5942–5949. https://doi.org/10.1109/LRA.2022.3160611.
14. Vergara, A., Lau, Y.S., Mendoza-Garcia, R.F., and Zagal, J.C. (2017). Soft modular robotic cubes: Toward replicating morphogenetic movements of the embryo. PLoS One *12*, e0169179. https://doi.org/10.1371/journal.pone.0169179.
15. Moreno, R., and Faiña, A. (2021). Emerge modular robot: A tool for fast deployment of evolved robots. Front. Robot. AI *8*. https://doi.org/10.3389/frobt.2021.699814. https://www.frontiersin.org/journals/robotics-and-ai/articles/10.3389/frobt.2021.699814.
16. Lee, J.Y., and Cho, K.J. (2017). Development of magnet connection of modular units for soft robotics. In 2017 14th International Conference on Ubiquitous Robots and Ambient Intelligence (URAI), pp. 65–67. https://doi.org/10.1109/URAI.2017.7992886.
17. Tapus, A., Mataric, M., and Scassellati, B. (2007). Socially assistive robotics [grand challenges of robotics]. IEEE Robot. Autom. Mag. *14*, 35–42. https://doi.org/10.1109/MRA.2007.339605.
18. Romanishin, J.W., Gilpin, K., and Rus, D. (2013). M-blocks: Momentum-driven, magnetic modular robots. In 2013 IEEE/RSJ International Conference on Intelligent Robots and Systems (IROS), pp. 4288–4295. https://doi.org/10.1109/IROS.2013.6696971.
19. Tosun, T., Davey, J., Liu, C., and Yim, M. (2016). Design and characterization of the ep-face connector. In 2016 IEEE/RSJ International Conference on Intelligent Robots and Systems (IROS), pp. 45–51. https://doi.org/10.1109/IROS.2016.7759033.
20. Davey, J., Kwok, N., and Yim, M. (2012). Emulating self-reconfigurable robots: Design of the smores system. In 2012 IEEE/RSJ International Conference on Intelligent Robots and Systems (IROS), pp. 4464–4469. https://doi.org/10.1109/IROS.2012.6385845.
21. Gilpin, K., Knaian, A., and Rus, D. (2010). Robot pebbles: One centimeter modules for programmable matter through self-disassembly. In 2010 IEEE International Conference on Robotics and Automation (ICRA), pp. 2485–2492. https://doi.org/10.1109/ROBOT.2010.5509817.
22. Daudelin, J., Jing, G., Tosun, T., Yim, M., Kress-Gazit, H., and Campbell, M. (2018). An integrated system for perception-driven autonomy with modular robots. Sci. Robot. *3*, eaat4983. https://doi.org/10.1126/scirobotics.aat4983.
23. Bray, E., and Groß, R. (2023). Recent developments in self-assembling multi-robot systems. Curr. Robot. Rep. *4*, 101–116. https://doi.org/10.1007/s43154-023-00106-y.
24. Knospler, J., Xue, W., and Trkov, M. (2024). A shared electrical-pneumatic and reversible locking intermodule connector for modular robots. In 2024 IEEE International Conference on Advanced Intelligent Mechatronics (AIM), pp. 160–165. https://doi.org/10.1109/AIM55361.2024.10637211.
25. Díaz-Carrasco Díaz, M., Guerra, G., Gala, J., and Viñals, J.J. (2023). Sirom electronics design: Current state and future developments. Acta Astronaut. *202*, 742–750. https://doi.org/10.1016/j.actaastro.2022.09.055. https://www.sciencedirect.com/science/article/pii/S009457652200532X.
26. SENER Group (n.d.). Standard interface for robotic manipulation (sirom). https://www.group.sener/en/project/standard-interface-robotic-manipulation-sirom#interface. . Accessed: 2025-03-27.
27. Guerra, G., Viñals, J., Soto, I., Díaz-Carrasco, M., and Gala, J. (2022). Development of a robotic fluid transfer interface based on rider connector. In Proc. Symposium on Advanced Space Technologies in Robotics and Automation (ASTRA).
28. Medina, A., Tomassini, A., Suatoni, M., Avilés, M., Solway, N., Coxhill, I., Paraskevas, I.S., Rekleitis, G., Papadopoulos, E., Krenn, R., et al. (2017). Towards a standardized grasping and refuelling on-orbit servicing for geo spacecraft. Acta Astronaut. *134*, 1–10. https://doi.org/10.1016/j.actaastro.2017.01.022. https://www.sciencedirect.com/science/article/pii/S0094576515302782.
29. Orbit F. (n.d.). Rafti: Rapidly attachable fluid transfer interface. https://www.orbitfab.com/rafti/. . Accessed: 2025-04-04.
30. Bian, X., Chen, W., Ran, D., Liang, Z., and Mei, X. (2023). Fima-reader: A cost-effective fiducial marker reader system for autonomous mobile robot

Please cite this article in press as: Wang and Stokes, Self-aligning EPM connector: A versatile solution for adaptive and multi-modal interfaces, Device (2026), https://doi.org/10.1016/j.device.2026.101068

docking in manufacturing environments. Appl. Sci. *13*, 13079. https://doi.org/10.3390/app132413079.

31. Alijani, F. (2017). Autonomous Vision-Based Docking of a Mobile Robot with Four Omnidirectional Wheels. Ph.D. thesis (Lund University). https://lup.lub.lu.se/luur/download?func=downloadFile&recordOId=8898960&fileOId=8898961studentPaper.
32. Knaian, A.N. (2010). Electropermanent Magnetic Connectors and Actuators: Devices and Their Application in Programmable Matter. Ph.D. thesis (Massachusetts Institute of Technology).
33. Padovani, J.I., Jeffrey, S.S., and Howe, R.T. (2016). Electropermanent magnet actuation for droplet ferromicrofluidics. Technology (Singapore World Science) *4*, 110–119. https://doi.org/10.1142/S2339547816500023.
34. Nakayama, Y., Van Ho, A., and Shibuya, K. (2024). Deformable soft tactile sensing system integrating electropermanent magnet and magnetorheological fluid. In 2024 IEEE/SICE International Symposium on System Integration (SII), pp. 60–65. https://doi.org/10.1109/SII58957.2024.10417588.
35. Kato, M., and Kitayama, F. (2023). Switchable frequency response based on electropermanent magnet actuator for wide-range operation of electromagnetic devices. IEEE Trans. Magn. *59*, 1–5. https://doi.org/10.1109/TMAG.2023.3276179.
36. McDonald, K.J., Kinnicutt, L., Moran, A.M., and Ranzani, T. (2022). Modulation of magnetorheological fluid flow in soft robots using electropermanent magnets. IEEE Robot. Autom. Lett. *7*, 3914–3921. https://doi.org/10.1109/LRA.2022.3147873.
37. Nagy, Z., Abbott, J.J., and Nelson, B.J. (2007). The magnetic self-aligning hermaphroditic connector: A scalable approach for modular microrobots. In 2007 IEEE/ASME International Conference on Advanced Intelligent Mechatronics (AIM), pp. 1–6. https://doi.org/10.1109/AIM.2007.4412519.